NASA Technical Paper 3313

May 1993

Performance Characteristics of Two Multiaxis Thrust-Vectoring Nozzles at Mach Numbers up to 1.28

David J. Wing
and Francis J. Capone

NASA Technical Paper 3313

1993

Performance Characteristics of Two Multiaxis Thrust-Vectoring Nozzles at Mach Numbers up to 1.28

David J. Wing
and Francis J. Capone
Langley Research Center
Hampton, Virginia

Summary

A thrust-vectoring axisymmetric (VA) nozzle and a spherical convergent flap (SCF) thrust-vectoring nozzle were tested along with a baseline nonvectoring axisymmetric (NVA) nozzle in the Langley 16-Foot Transonic Tunnel at Mach numbers from 0 to 1.28 and nozzle pressure ratios from 1 to 8. Test parameters included geometric yaw vector angle and unvectored divergent flap length. No pitch vectoring was studied. Nozzle drag, thrust minus drag, yaw thrust vector angle, discharge coefficient, and static thrust performance were measured and analyzed, as well as external static pressure distributions.

The NVA nozzle and the VA nozzle displayed higher static thrust performance and discharge coefficients than the SCF nozzle throughout the nozzle pressure ratio (NPR) range tested. The low discharge coefficients of the SCF nozzle were influenced by sharp corners at the nozzle throat. Increasing the divergent flap length under static conditions did not affect the internal performance of either the NVA nozzle or the SCF nozzle. The NVA nozzle had higher overall thrust minus drag than the other nozzles throughout the NPR and Mach number ranges tested. The SCF nozzle had the lowest jet-on nozzle drag of the three nozzles throughout the test conditions. At subsonic speeds, the SCF nozzle had better performance at lower values of NPR, and the VA nozzle had better performance at higher values of NPR. At supersonic speeds, the VA nozzle had higher performance at all NPR's tested. For the SCF nozzle, increasing the divergent flap length reduced the overall nozzle drag and increased the thrust minus drag throughout the Mach number range tested. The same was true for the NVA nozzle in supersonic flow. However, in subsonic flow, the thrust minus drag decreased, and the nozzle drag increased with nozzle length. The SCF nozzle provided yaw thrust vector angles that were equal to the geometric angle and constant with NPR. The VA nozzle achieved yaw thrust vector angles that were significantly higher than the geometric angle but not constant with NPR. Nozzle drag generally increased with increases in thrust vectoring for all the nozzles tested. A large increase in the SCF drag occurred as yaw vectoring was increased from 10° to 20°.

Introduction

Performance requirements for the future generation of fighter aircraft have established the need for improved agility and control in the high-angle-of-attack flight regime (ref. 1). In pursuit of this goal, research into augmenting aerodynamic control with engine-assisted control by vectoring the engine exhaust has been in progress for many years. Studies have shown that equipping a fighter aircraft with thrust-vectoring nozzles can increase its survivability by enhancing its maneuverability and turn rate (ref. 2). Attitude control that is independent of the aerodynamic control surfaces will also improve the nose-pointing capability of the aircraft in the high-angle-of-attack and poststall flight regimes. Thrust vectoring has also been shown to improve short field operations (ref. 3). Substantial research has been conducted into thrust-vectoring nozzles that provide pitch-only control (refs. 4 to 7). More recent efforts have been dedicated to developing efficient multiaxis (pitch plus yaw) thrust-vectoring nozzles in order to take full advantage of the benefits of the thrust-vectoring concept.

This report presents the results from a wind-tunnel study of the uninstalled performance of two basic multiaxis thrust-vectoring nozzle designs: a vectoring axisymmetric nozzle and a vectoring spherical convergent flap nozzle. The axisymmetric nozzle achieved thrust vectoring by deflection of only the divergent section of the nozzle (ref. 8) in the desired direction of thrust. The spherical convergent flap nozzle combined a ball-joint gimbaling mechanism for yaw vectoring and hinged, two-dimensional divergent flaps for pitch vectoring to achieve simultaneous multiaxis thrust vectoring (refs. 9 and 10). No pitch vectoring was studied in this investigation. A baseline nonvectoring axisymmetric nozzle was also tested for comparison.

This investigation was conducted in the Langley 16-Foot Transonic Tunnel on an isolated nacelle (no wings or tails) with propulsion simulation capability at Mach numbers from 0 to 1.28 and nozzle pressure ratios (NPR's) ranging from 1 to approximately 8, depending on Mach number. Angle of attack was held constant at 0°. The effects of varying nozzle divergent flap length and geometric yaw vector angle were studied.

Symbols

All forces and moments are referred to the stability axis system with the model moment reference center located at model station 42.390. The data reduction procedure and the aerodynamic force and moment terms and propulsion relationships used herein are discussed in reference 11.

A_e	nozzle exit area, in^2
A_i	cross-sectional area enclosed by seal strip, in^2

$A_{\max}$ maximum model cross-sectional area, in^2

A_t nozzle throat area, in^2

A_e/A_t nozzle expansion ratio

b reference length, 7.34 in.

C_D aft-end drag coefficient, $\frac{\text{Drag}}{q_o S}$, $C_D = C_{D-F}$ at NPR = 1 (jet off)

C_{D-F} drag-minus-thrust coefficient, $\frac{\text{Drag minus thrust}}{q_o S}$

$C_{D,n}$ nozzle drag coefficient, $\frac{D_n}{q_o S}$

C_F thrust coefficient along stability axis, $\frac{F}{p_a S}$

$C_{F,i}$ ideal thrust coefficient, $\frac{F_i}{p_a S}$

$C_{F,S}$ jet side-force coefficient, $\frac{F_S}{p_a S}$

C_n aft-end aerodynamic yawing-moment coefficient, $C_n = C_{n,t}$ at NPR = 1 (jet off)

$C_{n,j}$ jet yawing-moment coefficient, $\frac{\text{Yawing moment}}{p_a S}$

$C_{n,t}$ total aft-end yawing-moment coefficient, including thrust component, $\frac{\text{Yawing moment}}{q_o S b}$

C_p pressure coefficient, $\frac{p - p_o}{q_o}$

C_Y aft-end aerodynamic side-force coefficient, $C_Y = C_{Y,t}$ at NPR = 1 (jet off)

$C_{Y,t}$ total aft-end side-force coefficient including thrust component, $\frac{\text{Side force}}{q_o S}$

D drag

D_f friction drag on afterbody from MS 47.762 to MS 56.012

D_n nozzle drag including skin friction, lbf

D_p pressure drag on afterbody from MS 47.762 to MS 56.012

d_h height of SCF nozzle throat, in.

d_t throat diameter (or equivalent diameter for rectangular throat), in.

d_w width of SCF nozzle throat, in.

F measured thrust along stability axis, lbf

$F_{A,\text{bal}}$ axial force measured by force balance, lbf

$F_{A,\text{mom}}$ momentum tare axial force due to bellows, lbf

F_i ideal isentropic thrust, $w_p \sqrt{\frac{R_j T_{t,j}}{g^2} \frac{2\gamma}{\gamma - 1} \left[1 - \left(\frac{p_o}{p_{t,j}}\right)^{(\gamma-1)/\gamma}\right]}$, lbf

F_r measured resultant thrust, lbf

F_S measured jet side force, lbf

g gravitational constant, 32.174 ft/sec^2

L_f divergent flap length measured aft from nozzle throat to nozzle exit, in.

L_n length of nozzle measured from nozzle connect station to nozzle exit, in.

M Mach number

NPR nozzle pressure ratio, $\frac{p_{t,j}}{p_a}$ or $\frac{p_{t,j}}{p_o}$

$(\text{NPR})_{\text{des}}$ design nozzle pressure ratio

p local external static pressure, psia

p_a ambient pressure, psia

p_{es} average static pressure at external seal, psia

p_i average internal pressure, psia

p_o free-stream static pressure, psia

$p_{t,j}$ average jet total pressure, psia

q_o free-stream dynamic pressure, psia

R_j gas constant (for $\gamma = 1.3997$), $1716\ \text{ft}^2/\text{sec}^2\text{-}^\circ\text{R}$

r radius of body or nozzle, in.

r_a, r_b SCF nozzle radii (table 3(c)), in.

S model maximum cross-sectional area, $42.314\ \text{in}^2$

$T_{t,j}$ jet total temperature, °R

w_i ideal isentropic weight flow rate (for NPR > 1.89), $A_t p_{t,j} \left(\frac{2}{\gamma+1}\right)^{\frac{\gamma+1}{2(\gamma-1)}} \times \sqrt{\frac{\gamma g^2}{T_{t,j} R_j}}$, lbm/sec

w_p measured weight flow rate, lbm/sec

x	axial distance measured from nozzle connect station (MS 56.012), positive downstream, in.
YM	measured jet yawing moment, in-lb
y_a, z_b	coordinates for SCF nozzle radii (table 3(c)), in.
y'	lateral offset distance from model centerline to nozzle divergent passage centerline for vectored VA nozzles, positive to left looking upstream (fig. 5), in.
γ	ratio of specific heats, 1.3997 for air
$\delta_{v,y}$	geometric yaw vector angle, deg
δ_y	measured yaw thrust vector angle, $\tan^{-1}(F_S/F)$, deg
ϕ	angular location on model specifying location of static pressure tap rows (looking upstream, $\phi = -90°$ is left, $\phi = 0°$ is top, and $\phi = 90°$ is right), deg

Abbreviations:

C-D	convergent-divergent
MS	model station, in.
NVA	nonvectoring axisymmetric nozzle
SCF	spherical convergent flap nozzle
VA	vectoring axisymmetric nozzle
2-D	two-dimensional

Apparatus and Procedures

Wind Tunnel

This investigation was conducted in the Langley 16-Foot Transonic Tunnel, a single return, atmospheric tunnel with a slotted, octagonal test section and continuous air exchange. The wind tunnel has a variable airspeed up to a Mach number of 1.30. A complete description of this facility and its operating characteristics can be found in reference 12.

Single-Engine Propulsion Simulation System

The nozzles were tested on an isolated, single-engine propulsion simulation system that was mounted in the wind tunnel by a sting/strut support system. A photograph showing the installation of this system in the wind tunnel is shown in figure 1(a). A sketch of the propulsion simulation system is presented in figure 1(b). The axisymmetric forebody, which consisted of an ogive-cylinder up to MS 40.890, was nonmetric (not attached to the force balance). The metric portion of the model aft of MS 40.950, which was supported by the force balance, consisted of the propulsion system, centerbody, afterbody, and nozzles. All nozzles connected to the afterbody at MS 56.012. Table 1 presents the external geometry coordinates for both the fixed forebody and the metric afterbody up to MS 56.012. A 0.06-in. gap was placed between the fixed nonmetric forebody and the metric afterbody at MS 40.890 to prevent fouling of the force balance. A flexible plastic strip was inserted into circumferentially machined grooves in each component to impede flow into and out of the internal model cavity.

An external high-pressure air system provided a continuous source of clean, dry air at a controlled temperature of about 70°F at the nozzle. The air was routed through the sting/strut support system into the nacelle and through a flow transfer system to the nozzle. The flow transfer system, shown in figure 1(b), was designed to transfer the air to the metric portion of the model with minimal effect on the force balance. The air passed through the support strut and into a high-pressure plenum in the nacelle. The transfer across the balance was accomplished by discharging the air radially into a metric, low-pressure plenum through a set of eight, equally spaced, sonic nozzles. Two flexible metal bellows acted as seals and served to compensate for the axial forces caused by pressurization. The air then flowed through the plenum, into an instrumentation section, and out through the nozzle. This flow transfer system minimized the transfer of axial momentum from the airflow to the force balance.

Nozzles

Nozzle concepts. Two basic nozzle designs were tested in this investigation: an axisymmetric nozzle and a spherical convergent flap nozzle. Sketches of these nozzle concepts are shown in figure 2. The axisymmetric nozzle was subdivided into two groups: a nonvectoring axisymmetric (NVA) nozzle, similar to the type in use on current fighter aircraft, and a vectoring axisymmetric (VA) nozzle. The VA nozzle was similar in design to the NVA nozzle, except that multiaxis thrust vectoring was achieved by deflection of the divergent section of the nozzle. On a full-scale nonvectoring nozzle, the divergent section of the nozzle is made up of many overlapping flaps hinged at the throat (fig. 2). In the VA modified version, these

hinges are replaced with ball joints. Deflection of the divergent section flaps and seals into and away from the nozzle centerline is accomplished by push rods connected to a tilting synchronization ring. In order to accommodate the vectoring linkage and actuation mechanisms, an increase in nozzle volume is required, which results in a bulge in the external contour of the nozzle.

The spherical convergent flap (SCF) nozzle combined an axisymmetric cross section at the nozzle connect station with a two-dimensional (2-D) exit plane (fig. 2). This nozzle concept provided multiaxis thrust vectoring by deflecting the upper and lower divergent flaps for pitch control and gimbaling the entire nozzle about a ball joint in the horizontal plane for yaw control, allowing the nozzle sidewalls to be fixed. The axisymmetric and spherical convergent flap nozzles are both axisymmetric at their connect stations, providing structural efficiency and allowing the external shape to blend into the rounded engine nacelles on typical fighter afterbodies.

Nozzle models. The subscale nozzles tested during this investigation are fixed geometry representations of variable geometry nozzles at a dry power or cruise power setting. All nozzle configurations had a nominal throat area of approximately 6.7 in^2, an expansion ratio of 1.30, and a design NPR of 4.64. The configurations and some basic nozzle geometric data are listed in table 2. The nozzle geometric parameters studied in this investigation were divergent flap length and geometric yaw vector angle. In this report, divergent flap length is specified as a ratio to the nozzle throat diameter, L_f/d_t. Geometric yaw vector angles $\delta_{v,y}$ of 0°, 10°, and 20° for the VA and SCF nozzles were tested. The pitch vector angle was held constant at 0°.

A sketch of the nonvectoring axisymmetric nozzle is shown in figure 3, and external coordinates are given in table 3(a). The NVA nozzle was tested with divergent flap lengths of $L_f/d_t = 0.94$ and 1.42. A photograph of the nozzles is shown in figure 4. It is important to note, however, that the nozzle exit area was fixed. Therefore an increase in divergent flap length is accompanied by a decrease in both divergent flap angle and external boattail angle.

The vectoring axisymmetric nozzle is shown in the sketch of figure 5(a). The VA nozzle was tested only with a divergent flap length of $L_f/d_t = 0.94$ and with geometric yaw angles of 0°, 10°, and 20°. The difference between the unvectored VA nozzle and the NVA nozzle ($L_f/d_t = 0.94$) is shown in figure 5(b). The extra volume required for the synchronization ring (used for thrust vectoring) in the VA nozzle results in a bulge in the external contour. Photographs of the VA nozzles are shown in figure 6. External surface and centerline coordinates for the VA nozzles are presented in table 3(b).

The spherical convergent flap nozzle, shown in figure 7, was tested at $L_f/d_t = 0.94$, 1.20, and 1.46. It should be mentioned that the "effective" divergent flap length of the SCF nozzle would be shorter than the actual divergent flap length because the sidewalls were shorter than the 2-D flaps. The effective values of L_f/d_t of the SCF configurations, based on the average length of the sidewalls and flaps, would be 0.71, 0.90, and 1.10. Therefore, in this report, comparisons between the NVA, VA, and SCF nozzles were made at $L_f/d_t = 0.94$ for the NVA and VA nozzles and at $L_f/d_t = 1.20$ (effective ratio of 0.90) for the SCF nozzle. A comparison at these length ratios probably provides the most meaningful comparison between these nozzle configurations. The SCF nozzle with $L_f/d_t = 1.20$ was tested with yaw vector angles of 0°, 10°, and 20°. Photographs of these nozzle configurations are presented in figure 8. External nozzle coordinates are presented in table 3(c).

Instrumentation

Forces and moments on the afterbody and nozzle (aft of MS 40.950) were measured by a six-component strain-gauge balance. A critical-flow venturi system (ref. 13) outside the wind tunnel was used to measure total weight flow of air through the nozzle. Jet total pressure and total temperature were measured by probes in the instrumentation section immediately upstream of the nozzle. Pressures from nine total pressure probes, installed on a rake across the instrumentation section, were used to calculate an average total pressure for the jet. External-seal pressures were measured by six pressure taps in the seal gap at the metric break. All external seal orifices were located on the nonmetric forebody and were spaced symmetrically about the model perimeter. Four internal pressures were measured at the metric-gap station. These pressure measurements were then used to correct the measured forces and moments for pressure area tares, as discussed in the Data Reduction section. These pressures and the jet total pressures were measured with individual pressure transducers. Three rows of external static pressure taps were located on the upper and side surfaces of the afterbody and nozzle in order to determine the effects of nozzle geometry and exhaust jet interactions with external flow in the afterbody/nozzle region. The pressure tap distribution on the nozzles was not considered sufficient to perform an integrated pressure-area analysis

for the nozzles. Such an analysis was, however, performed for the afterbody to separate its drag contribution from that of the nozzles. The locations of the taps are tabulated in table 4. These pressures were measured with electronically scanning pressure devices.

Tests

This investigation was conducted in the Langley 16-Foot Transonic Tunnel at Mach numbers of 0.60, 0.80, 0.85, 0.90, 0.95, 1.20, and 1.28. Each thrust-vectoring nozzle was tested at Mach numbers of 0.60, 0.80, 0.90, and 1.20. Nozzle pressure ratio (nozzle total pressure to tunnel free-stream static pressure) was varied from 1 (jet off) to approximately 8, depending on the free-stream Mach number. Angle of attack was held at 0° throughout the test. The Reynolds number ranged from 3×10^6 to 4×10^6 per foot throughout the test. A boundary-layer transition strip, 0.10 in. wide, consisting of No. 100 silicon carbide grit sparsely distributed in a lacquer film, was applied 1.0 in. downstream of the nose.

Surface flow visualization data were obtained for the 10° yaw-vectored SCF nozzle by using a mixture of linseed oil paint, tempera paint, and kerosene. Data were obtained at Mach 0.70 with the jet on. The tunnel flow evaporated the kerosene, leaving a residue showing the surface flow patterns on the model. Although analysis based on this type of flow visualization is fairly subjective, it can provide insight into the flow behavior on and near the painted surface (ref. 14).

Data Reduction

Data from both the model and the wind-tunnel instrumentation were recorded simultaneously on magnetic tape. At each test point, 50 samples of data were recorded over a 5-sec period. The samples were averaged, and these average values were used for all computations. All aerodynamic coefficients were referenced to model maximum cross-sectional area (42.314 in^2).

The balance force measurements, from which actual thrust was subsequently obtained, were corrected for model weight tares and balance interactions. Although the bellows arrangement was designed to eliminate pressure and momentum interactions with the balance, small bellows tares on all balance components still exist. These residual tares result from a small pressure difference between the ends of the bellows when internal velocities are high and also from small differences in the forward and aft bellows spring constants when the bellows are pressurized. As described in reference 12, these bellows (momentum) tares were determined by testing calibration nozzles with known performance over a range of expected side-force and yawing-moment loadings. The balance data were then corrected in a manner similar to that discussed in reference 11.

At static conditions, the resultant gross thrust F_r (used in the resultant thrust ratio F_r/F_i) was then determined from the individual corrected forces F and F_s and ideal thrust F_i, defined for isentropic flow in the Symbols section of this report. Resultant thrust vector angle δ_y, also defined in the Symbols section, is presented for evaluating the exhaust-flow turning capabilities of the various nozzles tested.

Nozzle discharge coefficient w_p/w_i is the ratio of measured weight flow rate to ideal weight flow rate, where ideal weight flow is based on jet total pressure $p_{t,j}$, jet total temperature $T_{t,j}$, and measured nozzle throat area A_t (see Symbols section). Nozzle discharge coefficient is then a measure of the ability of the nozzle to pass weight flow and is reduced by boundary-layer thickness and nonuniform flow in the throat.

At wind-on conditions, thrust minus drag was obtained from the following equation:

$$F - D = F_{A,\text{bal}} + (p_{es} - p_o)(A_{\max} - A_i) + (p_i - p_o)A_i - F_{A,\text{mom}}$$

The first term, $F_{A,\text{bal}}$, includes all pressure and viscous forces (internal and external on the afterbody and nozzle and thrust system). The second and third terms account for the exterior and interior pressure forces acting at the metric break. The fourth term, $F_{A,\text{mom}}$, is the momentum (bellows) tare force previously discussed. Thrust minus nozzle drag is then determined from the equation

$$F - D_n = (F - D) + D_f + D_p$$

where the last two terms are the friction drag and pressure drag (integrated from static pressure measurements) of the afterbody from MS 40.950 (metric break) to MS 56.012 (nozzle connect station).

The attitude of the nonmetric forebody was determined by a calibrated attitude indicator in the model nose. Angle of attack, which is the angle between the afterbody/nozzle centerline and the relative wind, was determined by applying terms for afterbody deflection (caused when the model and balance bend under aerodynamic load) and a term for tunnel flow angularity to the angle measured by the attitude indicator. The tunnel flow angularity

correction was 0.1°, which is the average upflow angle measured in the 16-Foot Transonic Tunnel (ref. 12).

The thrust-removed (nozzle) aerodynamic forces and moments were obtained by determining the components of thrust in axial force, side force, and yawing moment and then subtracting these values from the measured total (aerodynamic plus thrust) forces and moments. These thrust components at forward speeds were determined from measured static data and were a function of the free-stream static and dynamic pressures.

Presentation of Results

The results of this investigation are presented in both tabular form and plotted form. Static and aeropropulsive performance data for all the nozzle configurations tested are presented in tables 5 to 14. Tables 15 to 24 present external static pressure coefficient data for these same configurations. Two parameters are used to illustrate the effects of varying nozzle geometric parameters on the nonvectored nozzle performance characteristics: the aeropropulsive performance parameter $(F - D_n)/F_i$ and the nozzle drag coefficient $C_{D,n}$. These data are shown as functions of nozzle pressure ratio for each of the Mach numbers tested. These two parameters are also summarized as functions of Mach number at a nozzle pressure ratio of 4.5, near the design NPR of 4.64. Although discussion of the results at this pressure ratio and Mach number would generally be applicable to other nozzle pressure ratios, the relative difference between comparisons may vary. Data for various nozzle configurations are presented in figures 9 to 34 as follows:

Discussion of Results

Nozzle Static Performance—Nonvectored

Comparison of NVA, VA, and SCF nozzles. The internal performance of the nonvectoring axisymmetric (NVA), the vectoring axisymmetric (VA), and the spherical convergent flap (SCF) nozzles in the unvectored configuration is shown in figure 9. All three nozzles exhibited the static thrust behavior of typical convergent-divergent nozzles. At low NPR's, the resultant thrust ratio of each nozzle increased rapidly with increasing NPR, reaching a maximum value at NPR $\approx$ 5.5, and gradually decreased at higher NPR's. The design NPR of a convergent-divergent nozzle can be determined from isentropic theory by using the area ratio from the throat to the exit plane; it is the NPR at which the flow should be fully expanded and peak thrust performance should occur. All the nozzles had an expansion ratio of approximately 1.3, corresponding to a design NPR of approximately 4.64. The NVA and VA nozzles reached their peak resultant thrust ratios between NPR = 5 and 6. The SCF nozzle reached its peak resultant thrust ratio closer to NPR = 6. The low value of discharge coefficient of the SCF nozzle, shown in the same figure, reflects a smaller effective flow area at the throat, which in turn would increase the effective exit-to-throat area ratio and cause optimum performance to shift to a higher NPR. The low value of discharge coefficient of the SCF nozzle is probably the result of the flow not being able to negotiate the sharp turn at the throat (close to 90° on the upper and lower surfaces, as shown in figure 7). A separation bubble forming at the throat would reduce the effective area for passing the exhaust. It should be noted that the exact exit area of the SCF nozzle to be used for analysis cannot be determined, because the walls of the divergent flap are of unequal length. Previous investigations into shortening the sidewalls of 2-D C-D nozzles have been inconclusive as to the effect on the effective expansion ratio (refs. 7 and 15).

The NVA nozzle displayed the highest resultant thrust performance of the three nozzles. The unvectored thrust performance and discharge coefficients of the VA nozzle were close to those of the NVA nozzle, which was expected, as the internal geometries were designed to be virtually the same. The SCF nozzle had the lowest internal performance of the three nozzles, most likely a result of the sharp corner at the nozzle throat. SCF nozzles with rounded corners at the throat have been shown to have higher internal performance than those with sharp corners (ref. 10).

Effect of divergent flap length. The effect of varying divergent flap length on the static internal performance of the NVA nozzle and the unvectored SCF nozzle is shown in figures 10 and 11, respectively. The resultant thrust ratio was not affected by varying the divergent flap length of either nozzle. Increasing the flap length of the NVA nozzle resulted in a small apparent increase in discharge coefficient. The increase was likely a function of the accuracy of the geometric throat area measurement. Once the nozzle reaches the "choke" NPR (approximately 1.89), its weight flow characteristics are fixed, and geometric alterations downstream of the throat cannot feed upstream through the supersonic flow. The discharge coefficient of the SCF nozzle, shown in figure 11, was also negligibly affected by lengthening the flaps.

Performance at Forward Speeds—Nonvectored

Comparison of NVA, VA, and SCF nozzles. The aeropropulsive performance and nozzle drag coefficients for the NVA, VA, and SCF nozzles are shown in figures 12 to 15. Figures 12 and 14 contain the thrust-minus-nozzle-drag and nozzle drag data at all NPR's and Mach numbers tested. These data are summarized in figures 13 and 15 at NPR = 4.5. Figure 15 includes a summary plot of jet-off nozzle drag coefficients. The NVA and VA nozzle data presented in these figures are for divergent flap lengths of $L_f/d_t = 0.94$. The data for the SCF nozzle are presented for the $L_f/d_t = 1.20$ flap length. As discussed earlier, this nozzle has an equivalent length ratio of $L_f/d_t = 0.90$ (arrived at by averaging the lengths of the sidewalls and flaps), making this nozzle an appropriate choice for comparison with the other two nozzles.

The NVA nozzle had equal or higher thrust minus nozzle drag than the other two nozzles at almost all Mach numbers and pressure ratios tested (fig. 12). The higher performance for the NVA nozzle is mainly a result of this nozzle having greater thrust (fig. 9) and, in some cases, lower drag than the other two nozzles. Of the SCF and VA nozzles at subsonic speeds, the SCF nozzle had the better performance at lower values of NPR, whereas the VA nozzle had the better performance at higher values of NPR. At supersonic speeds, the SCF nozzle always had the lowest thrust-minus-nozzle-drag data throughout the NPR range tested.

A summary of thrust-minus-nozzle-drag data at NPR = 4.5 (near design) is presented in figure 13. Above $M = 1$, the NVA and VA nozzles have equal

performance, superior to the SCF performance. (The low magnitude of thrust minus drag is indicative of high supersonic drag.) Below $M = 1$, the NVA and VA nozzles again are superior in performance to the SCF nozzle except at $M = 0.95$. Here, the VA performance decreases, suggesting an early transonic drag rise.

Nozzle drag data at all Mach numbers and NPR's tested are presented in figure 14. At nearly all jet-on test conditions, the SCF nozzle had the lowest drag of the three nozzle designs. Unfortunately, low internal performance resulted in the low thrust-minus-drag performance seen in figure 13.

Nozzle drag is summarized in figure 15 for both NPR = 1 (jet off) and NPR = 4.5 (near design). A transonic drag rise is observed for the VA nozzle initiating at approximately $M = 0.90$. Blowing the jet has the effect of reducing the nozzle drag at Mach numbers between 0.80 and 0.90; however, the drag rise at $M = 0.90$ is not affected. No similar transonic drag rise is observed for the other nozzles. Again, one observes that at all transonic Mach numbers, the SCF nozzle has the lowest jet-on nozzle drag.

External static pressure distributions for the three nozzle configurations are shown in figure 16 for Mach numbers of 0.60, 0.90, and 1.20 at NPR = 1 (jet-off conditions) and at NPR = 4.5 (near design). The results at the other Mach numbers tested are similar. For reference, the nozzle connect station is at $x/L_n = 0$ (MS 56.012); negative values of x/L_n are for pressures on the afterbody (upstream), and positive values are on the nozzle (downstream). These pressure distributions exhibit expected trends. There was a slight expansion of the flow along the afterbody, which is consistent with the fact that the afterbody surface has a small boattail angle. A stronger expansion is indicated near the nozzle connect station, followed by a pressure recovery sufficiently strong enough in the subsonic cases to produce positive pressure coefficients (negative nozzle drag or thrust). Base bleeding effects will cause an increase in the static pressure coefficients with initial jet operation. Thereafter, NPR has little or no effect on the static pressures.

The pressure data for the VA nozzle indicate that the flow expansion occurs farther aft than for the NVA or SCF nozzles. The delay in expansion is the result of the external contour modification required to house the vectoring mechanism.

Effect of NVA nozzle divergent flap length. The effect of varying the divergent flap length of the NVA nozzle on the aeropropulsive parameter $(F - D_n)/F_i$ and nozzle drag C_D is presented in figures 17 to 20. As can be seen in figures 17 and 18, increasing the divergent flap length resulted in a decrease in $(F - D_n)/F_i$ at subsonic speeds and an increase in $(F - D_n)/F_i$ at supersonic speeds. The changes in performance are mainly the result of differences in nozzle drag, since these nozzles have similar thrust characteristics (fig. 10). As can be seen in the data set in figure 19 and the summary data in figure 20, the nozzle drag coefficient of the shorter nozzle was equal to or less than that of the longer nozzle at subsonic speeds but significantly greater at supersonic speeds.

Afterbody/nozzle surface pressure distributions for the short and long NVA nozzles are presented in figure 21. The main effects of increasing divergent flap length were a reduction in the expansion region around the nozzle shoulder and a pressure recovery to lower pressures at the trailing edge. The short NVA nozzle had a steeper boattail angle than the long nozzle because the exit area was fixed. The higher pressure acting on the steep boattail surface, combined with lower skin friction drag (less wetted area), resulted in lower subsonic drag for the shorter nozzle. At supersonic speeds, the increase in nozzle drag for the shorter nozzle is probably the result of the stronger initial expansion of the flow that occurs at the nozzle shoulder.

Effect of SCF nozzle divergent flap length. The effect of flap length on the aeropropulsive parameter for the SCF nozzle is shown in the data set of figure 22 and the summary data of figure 23. At both subsonic and supersonic speeds, $(F - D_n)/F_i$ generally increased with increasing flap length. This behavior was primarily the result of changes in nozzle drag rather than thrust, since these nozzles have essentially the same thrust characteristics (fig. 11). The drag data shown in figures 24 and 25 indicate that the SCF nozzle with the longest flap generally had the lowest overall drag at all speeds. This result differs from the result discussed previously for the NVA nozzles, in which the longer nozzle had lower nozzle drag only at supersonic speeds. A study of the surface pressure distributions of the SCF nozzle in figure 26 shows that the shorter nozzle (with larger boattail angle) did not have higher pressures acting on the boattail at subsonic speeds in contrast to the NVA nozzle. As discussed earlier, this pressure distribution on the shorter NVA nozzle resulted in lower subsonic nozzle drag. The shorter SCF nozzle did not have this pressure advantage and therefore had higher subsonic drag. The upper flap pressure distribution was the most predominantly

affected, and therefore only those pressure coefficients are presented in this figure.

At high subsonic and supersonic speeds, the pressure recovery on the short flap nozzle was weakest (smallest value of C_p), resulting in higher pressure drag. Closer examination of the pressure distribution on the short flap nozzle with the jet on suggests a possible flow separation, as evidenced by the flattened pressure coefficient profile near the trailing edge. All the SCF nozzles have the same exit area, and therefore the nozzle having the shortest flap length has the largest boattail angle. Surfaces with large boattail angles are more likely to have flow separation, as low energy flow cannot negotiate large angle turns.

Nozzle Static Performance—Vectored

VA nozzle. The static internal performance for the VA nozzle at yaw vectoring angles of 0°, 10°, and 20° is shown in figure 27. Testing of the VA nozzle at a yaw angle of 20° was restricted to pressure ratios at NPR $\leq$ 3.5 because of force balance limitations. The VA nozzle displayed an increase in resultant thrust ratio with increases in yaw vectoring. This behavior has been documented in previous studies, including a 2-D C-D nozzle (ref. 16), a gimballed axisymmetric nozzle (ref. 9), and a vectoring axisymmetric nozzle similar to the VA nozzle of this investigation (ref. 8). The decrease in F/F_i in figure 27 as the geometric vector angle is increased from 0° to 10° is consistent with the thrust loss expected from deflecting the thrust approximately 10° away from the nozzle axis. However, yaw thrust vector angles significantly greater than 10° were measured, indicating some overturning of the flow or the existence of additional pressure loads on the nozzle surfaces. The precise nature of the increase in performance is not well understood. The behavioral trends in static thrust are, however, consistent with the trends published in the static test of a similar configuration in reference 8.

The resultant yaw thrust vector angles shown in figure 27 increased rapidly with increasing NPR at low pressure ratios to angles significantly greater than the geometric yaw angle of the nozzle. Accordingly, axial thrust ratio F/F_i decreased with increasing NPR. Similar results were found for a similar VA nozzle configuration in reference 8. Internal static pressure measurements in that investigation showed regions of significant flow separation on the leeward (aft-facing) divergent internal nozzle surface at low NPR's. Substantial increases in turning efficiency were obtained as NPR was increased to a level sufficient to eliminate the separated region. At and above this NPR, as in this investigation, thrust vector angles well above the geometric angle were measured.

Once the maximum thrust vector angle was achieved, δ_y decreased slowly with increases in NPR. This effect of nozzle pressure ratio on thrust angularity is common in nonaxisymmetric nozzles whenever one flap is longer than the other relative to the exhaust flow centerline (ref. 17). In the present investigation, one side of the divergent channel extends farther downstream than the opposite side, in relation to the exhaust flow centerline. This type of nozzle geometry presents surfaces of unequal length for flow expansion, such that near the nozzle exit, the exhaust flow is contained on one side and unbounded on the other side. It is expected that the nozzle vectored 20° would have similar trends with NPR as the nozzle vectored 10°. Again, balance limitations restricted the test range of the $\delta_{v,y} = 20°$ configuration. Discharge coefficient was adversely affected by increasing the yaw vectoring angle, most likely a result of a reduction in effective throat area possibly caused by a local region of flow separation.

SCF nozzle. The static internal performance of the SCF nozzle at yaw vectoring angles of 0°, 10°, and 20° is shown in figure 28. As was also seen for the VA nozzle, the resultant thrust ratio of the SCF nozzle increased as the geometric vectoring angle was increased, most significantly from 10° to 20°. A previous investigation of a similar SCF nozzle (ref. 9) showed slight increases of resultant thrust ratio with increased yaw vectoring at positive pitch deflection angles, but no significant effect was noted at a pitch deflection angle of 0°. Again, the reason for this increase in efficiency is not well understood. The SCF nozzle provided constant turning angles equal to the geometric angle at all pressure ratios, as shown in the lower left plot of figure 28, because of its gimbaling concept for thrust vectoring. Discharge coefficient was unaffected by yaw vectoring.

Comparison of VA and SCF nozzles. The performance of the VA and SCF nozzles is shown in figure 29. The distinction between the performance characteristics of the two nozzle designs can be clearly seen in the yaw thrust vector angle data (δ_y). The SCF design, utilizing a gimbal, provides constant turning at the prescribed geometric angle, whereas the VA nozzle exceeds the geometric angle at the cost of independence from NPR. In a comparison of axial thrust, the SCF nozzle has a smooth performance curve, which is conventional C-D nozzle behavior, whereas the VA nozzle sacrifices a smooth performance curve for slightly higher efficiency, for

$\delta_{v,y} = 10°$ (which is the only significant comparison available in this data set).

Performance at Forward Speeds—Vectored

VA nozzle. The total and thrust-removed aerodynamic characteristics of the VA nozzle at $\delta_{v,y} = 0°$, 10°, and 20° are presented in figure 30. Data are presented at Mach numbers of 0.60 and 0.90 only, as the characteristics at the other Mach numbers tested were similar. All data, however, are tabulated in this report.

In this section, data are presented in coefficient format rather than performance efficiency (ratio to ideal behavior) format because actual forces and moments produced by the nozzle are of interest in wind-on thrust vectoring. Drag-minus-thrust coefficient C_{D-F} varies linearly with NPR. Increases in C_{D-F} with increased vectoring are the result of a reduction in the axial thrust component as the thrust vector is turned away from the nozzle centerline.

Aft-end drag coefficient C_D is computed by removing the static thrust from the wind-on drag-minus-thrust data and is also presented in figure 30. Aft-end drag of the VA nozzle with $\delta_{v,y} = 10°$ exceeds that of the nozzles with $\delta_{v,y} = 0°$ and 20°. The aft-end pressure distributions shown in figure 31 do not give much insight into the reason for this behavior. The pressure distributions show separated regions (flat distributions) on the leeward side ($\phi = 90°$) of both the $\delta_{v,y} = 10°$ and $\delta_{v,y} = 20°$ nozzles and significant jet-induced effects on the distributions on the windward ($\phi = -90°$) side of the nozzles. The higher pressure on the windward side of the $\delta_{v,y} = 20°$ nozzle (jet on) as compared with the $\delta_{v,y} = 10°$ nozzle could possibly result in reduced aft-end drag, although the aft-facing surface area on the windward side of the $\delta_{v,y} = 20°$ nozzle is small.

Total side-force coefficient $C_{Y,t}$ and total yawing-moment coefficient $C_{n,t}$, for the VA nozzle, are presented in figure 30 as well. Removing the thrust contribution from these coefficients by using the static data yields the side-force and yawing-moment coefficients, C_Y and C_n; these coefficients represent aerodynamic and jet-induced contributions to the side force and yawing moments. As shown in figure 30, these contributions were small but were generally favorable because they acted in the same direction as thrust. The higher pressure on the windward side ($\phi = -90°$), shown in figure 31, produced a net side force at the nozzle, adding to the lateral jet component.

SCF nozzle. The total and thrust-removed aerodynamic characteristics of the SCF nozzle at $\delta_{v,y} = 0°$, 10°, and 20° are presented in figure 32, again only at $M = 0.60$ and 0.90. As with the VA nozzle, the drag-minus-thrust coefficients varied linearly with NPR and included the effect of turning the thrust vector away from the nozzle axis. In the case of the SCF nozzle, the aft-end drag increased with increased yaw vectoring, with a large increase from $\delta_{v,y} = 10°$ to $\delta_{v,y} = 20°$. Flow features identified in the static pressure distributions shown in figure 33 are higher pressures on the windward side ($\phi = -90°$) and possible shock-induced separation on the leeward side of the nozzle ($\phi = 90°$).

The linear behavior of total side-force and total yawing-moment coefficients, $C_{Y,t}$ and $C_{n,t}$, with NPR (see fig. 32) was similar to that for the VA nozzle. The thrust-removed coefficients, however, show a more significant aerodynamic flap effect as compared with the VA nozzle. Again, the difference between windward and leeward pressure distributions shown in figure 33 created a net favorable side force on the nozzle. The jet-induced effects were small, as C_Y and C_n were fairly constant with NPR.

Comparison of VA and SCF nozzles. The total side-force and yawing-moment coefficients of the VA and SCF nozzles are shown in figure 34 at $\delta_{v,y} = 10°$ and 20°, for $M = 0.60$ and 0.90. At $\delta_{v,y} = 10°$, the behaviors of $C_{Y,t}$ and $C_{n,t}$ as functions of NPR are more linear for the SCF nozzle than for the VA nozzle. At $\delta_{v,y} = 20°$, the $C_{Y,t}$ and $C_{n,t}$ curves of the VA nozzle become more linear as well. The force and moment curves cross each other between NPR = 2 and NPR = 4, such that at low NPR, the SCF nozzle produces larger side forces and yawing moments, and at high NPR, the VA nozzle produces the larger loads.

Surface flow visualization. The SCF nozzle at 10° yaw vectoring was painted with an oil-based paint for surface flow visualization. The Mach number was set at $M = 0.70$ with the jet on. Although analysis using this technique is considered highly subjective, certain useful observations can be made. A side view of the windward nozzle surface (turned toward the free-stream flow) is presented in figure 35(a). This figure shows what appears to be smooth, attached flow over the majority of the sidewall with some spillage onto the upper and lower flaps. The opposite (leeward) side of the nozzle is shown in figure 35(b). Here, large eddy regions are apparent on most of the nozzle surface, confirming the flow separation suggested by the pressure distribution shown in figure 33. A rather distinct line of

separation can be seen just downstream of the third pressure orifice. The top and bottom surfaces are shown in figures 35(c) and 35(d), respectively. A line of attachment is apparent along each windward edge. This feature, along with the spillage seen on the windward nozzle surface, suggests a rolled up, longitudinal vortex. The surface pattern also suggests that the flow near the surface aligned itself with the nozzle flap, probably a result of flow entrainment with the jet.

Conclusions

An investigation has been conducted in the Langley 16-Foot Transonic Tunnel to determine the isolated performance of a nonvectoring axisymmetric (NVA) nozzle, a vectoring axisymmetric (VA) nozzle, and a spherical convergent flap (SCF) nozzle. Nozzle geometric parameters studied included divergent flap length and geometric yaw thrust vector angle. The nozzles were tested at Mach numbers ranging from 0 to 1.28 and nozzle pressure ratios (NPR's) ranging from 1 to 8. Based on the discussion of results presented in this paper, the following conclusions are made:

1. The NVA nozzle and the unvectored VA nozzle displayed higher static (wind-off) thrust performance and discharge coefficients than the SCF nozzle throughout the NPR range tested. The SCF nozzle had significantly lower discharge coefficients than the axisymmetric nozzles, possibly because of sharp corners at the nozzle throat.
2. Increasing the divergent flap length under static conditions had a negligible effect on the thrust performance of the NVA and SCF nozzles.
3. The NVA nozzle had higher overall thrust minus drag than the other nozzles throughout the NPR and Mach number ranges tested. At subsonic speeds, the SCF nozzle had the better performance at lower values of NPR, and the VA nozzle had the better performance at higher values of NPR. At supersonic speeds, the VA nozzle had higher performance at all NPR's tested.
4. For the SCF nozzle, increasing the divergent flap length reduced the overall nozzle drag and increased the thrust minus drag throughout the Mach number range tested. The same was true for the NVA nozzle in supersonic flow. However, in subsonic flow, the thrust minus drag decreased, and the nozzle drag increased with nozzle length, partially because of a reduction in pressure recovery on the boattail.
5. The SCF nozzle provided yaw thrust vector angles equal to the geometric angle and constant with NPR. The VA nozzle achieved yaw thrust vector angles that were significantly higher than the geometric angle but not constant with NPR.
6. Nozzle drag increased with increases in thrust vectoring for all the nozzles tested, with the exception of the VA nozzle as yaw vectoring was increased from 10° to 20°. A large increase in the SCF nozzle drag occurred as yaw vectoring was increased from 10° to 20°. Aerodynamic flap contributions to the yawing-moment coefficient and side-force coefficient from yaw vectoring were significant for the SCF nozzle.

NASA Langley Research Center
Hampton, VA 23681-0001
March 19, 1993

References

1. Herbst, W. B.: Future Fighter Technologies. *J. Aircr.*, vol. 17, no. 8, Aug. 1980, pp. 561–566.
2. Tamrat, B. F.: Fighter Aircraft Agility Assessment Concepts and Their Implication on Future Agile Fighter Design. AIAA-88-4400, Sept. 1988.
3. Ward, B. D.; and Lewis, W. J.: Advantages of Thrust Vectoring for STOVL. AIAA-87-1708, June–July 1987.
4. Capone, Francis J.: *Static Performance of Five Twin-Engine Nonaxisymmetric Nozzles With Vectoring and Reversing Capability.* NASA TP-1224, 1978.
5. Capone, Francis J.; and Berrier, Bobby L.: *Investigation of Axisymmetric and Nonaxisymmetric Nozzles Installed on a 0.10-Scale F-18 Prototype Airplane Model.* NASA TP-1638, 1980.
6. Leavitt, Laurence D.: Summary of Nonaxisymmetric Nozzle Internal Performance From the NASA Langley Static Test Facility. AIAA-85-1347, July 1985.
7. Capone, Francis J.; Mason, Mary L.; and Leavitt, Laurence D.: *An Experimental Investigation of Thrust Vectoring Two-Dimensional Convergent-Divergent Nozzles Installed in a Twin-Engine Fighter Model at High Angles of Attack.* NASA TM-4155, 1990.
8. Carson, George T., Jr.; and Capone, Francis J.: *Static Internal Performance of an Axisymmetric Nozzle With Multiaxis Thrust-Vectoring Capability.* NASA TM-4237, 1991.
9. Berrier, Bobby L.; and Taylor, John G.: *Internal Performance of Two Nozzles Utilizing Gimbal Concepts for Thrust Vectoring.* NASA TP-2991, 1990.
10. Taylor, John G.: *Internal Performance of a Hybrid Axisymmetric/Nonaxisymmetric Convergent-Divergent Nozzle.* NASA TM-4230, 1991.

11. Mercer, Charles E.; Berrier, Bobby L.; Capone, Francis J.; Grayston, Alan M.: *Data Reduction Formulas for the 16-Foot Transonic Tunnel: NASA Langley Research Center, Revision 2.* NASA TM-107646, 1992. (Supersedes NASA TM-86319, Revision 1, 1987.)

12. Staff of the Propulsion Aerodynamics Branch: *A User's Guide to the Langley 16-Foot Transonic Tunnel Complex, Revision 1.* NASA TM-102750, 1990.

13. Berrier, Bobby L.; Leavitt, Laurence D.; and Bangert, Linda S.: *Operating Characteristics of the Multiple Critical Venturi System and Secondary Calibration Nozzles Used for Weight-Flow Measurements in the Langley 16-Foot Transonic Tunnel.* NASA TM-86405, 1985.

14. Maltby, R. L.; and Keating, R. F. A.: The Surface Oil Flow Technique for Use in Low Speed Wind Tunnels. *Flow Visualization in Wind Tunnels Using Indicators,* R. L. Maltby, compiler, AGARDograph 70, Apr. 1962, pp. 29–38.

15. Yetter, Jeffery A.; and Leavitt, Laurence D.: *Effects of Sidewall Geometry on the Installed Performance of Nonaxisymmetric Convergent-Divergent Exhaust Nozzles.* NASA TP-1771, 1980.

16. Capone, Francis J.; and Bare, E. Ann: *Multiaxis Control Power From Thrust Vectoring for a Supersonic Fighter Aircraft Model at Mach 0.20 to 2.47.* NASA TP-2712, 1987.

17. Re, Richard J.; and Leavitt, Laurence D.: *Static Internal Performance Including Thrust Vectoring and Reversing of Two-Dimensional Convergent-Divergent Nozzles.* NASA TP-2253, 1984.

Table 5. Static and Aeropropulsive Characteristics for NVA Nozzle; $L_f/d_t = 0.94; \delta_{v,y} = 0°$

(a) Static performance

(b) Aeropropulsive characteristics

Table 6. Static and Aeropropulsive Characteristics for NVA Nozzle; $L_f/d_t = 1.42; \delta_{v,y} = 0°$

(a) Static performance

(b) Aeropropulsive characteristics

Table 7. Static and Aeropropulsive Characteristics for VA Nozzle; $L_f/d_t = 0.94; \delta_{v,y} = 0°$

(a) Static performance

(b) Aeropropulsive characteristics

Table 8. Static and Aeropropulsive Characteristics for VA Nozzle; $L_f/d_t = 0.94; \delta_{v,y} = 10°$

(a) Static performance

(b) Aeropropulsive characteristics

Table 9. Static and Aeropropulsive Characteristics for VA Nozzle; $L_f/d_t = 0.94; \delta_{v,y} = 20°$

(a) Static performance

(b) Aeropropulsive characteristics

Table 10. Static and Aeropropulsive Characteristics for SCF Nozzle; $L_f/d_t = 1.20; \delta_{v,y} = 0°$

(a) Static performance

(b) Aeropropulsive characteristics

Table 11. Static and Aeropropulsive Characteristics for SCF Nozzle; $L_f/d_t = 1.20; \delta_{v,y} = 10°$

(a) Static performance

(b) Aeropropulsive characteristics

Table 12. Static and Aeropropulsive Characteristics for SCF Nozzle; $L_f/d_t = 1.20; \delta_{v,y} = 20°$

(a) Static performance

(b) Aeropropulsive characteristics

Table 13. Static and Aeropropulsive Characteristics for SCF Nozzle; $L_f/d_t = 0.94; \delta_{v,y} = 0°$

(a) Static performance

(b) Aeropropulsive characteristics

Table 14. Static and Aeropropulsive Characteristics for SCF Nozzle; $L_f/d_t = 1.46; \delta_{v,y} = 0°$

(a) Static performance

(b) Aeropropulsive characteristics

Table 15. Static Pressure Coefficients for NVA Nozzle; $L_f/d_t = 0.94; \delta_{v,y} = 0°$

(a) $\phi = -90°$

Static pressure coefficients for x/L_n of—

Table 15. Continued

(b) $\phi = 0°$

Static pressure coefficients for x/L_n of—

Table 15. Concluded

(c) $\phi = 90°$

Static pressure coefficients for x/L_n of—

Table 16. Static Pressure Coefficients for NVA Nozzle; $L_f/d_t = 1.42; \delta_{v,y} = 0°$

(a) $\phi = -90°$

Static pressure coefficients for x/L_n of—

Table 16. Continued

(b) $\phi = 0°$

Static pressure coefficients for x/L_n of—

Table 16. Concluded

(c) $\phi = 90°$

Static pressure coefficients for x/L_n of—

Table 17. Static Pressure Coefficients for VA Nozzle; $L_f/d_t = 0.94; \delta_{v,y} = 0°$

(a) $\phi = -90°$

Static pressure coefficients for x/L_n of—

Table 17. Continued

(b) $\phi = 0°$

Static pressure coefficients for x/L_n of—

Table 17. Concluded

(c) $\phi = 90°$

Static pressure coefficients for x/L_n of—

Table 18. Static Pressure Coefficients for VA Nozzle; $L_f/d_t = 0.94; \delta_{v,y} = 10°$

(a) $\phi = -90°$

Static pressure coefficients for x/L_n of—

Table 18. Continued

(b) $\phi = 0°$

Static pressure coefficients for x/L_n of—

Table 18. Concluded

(c) $\phi = 90°$

Static pressure coefficients for x/L_n of—

Table 19. Static Pressure Coefficients for VA Nozzle; $L_f/d_t = 0.94; \delta_{v,y} = 20°$

(a) $\phi = -90°$

Static pressure coefficients for x/L_n of—

Table 19. Continued

(b) $\phi = 0°$

Static pressure coefficients for x/L_n of—

Table 19. Concluded

(c) $\phi = 90°$

Static pressure coefficients for x/L_n of—

Table 20. Static Pressure Coefficients for SCF Nozzle; $L_f/d_t = 1.20; \delta_{v,y} = 0°$

(a) $\phi = -90°$

Static pressure coefficients for x/L_n of—

Table 20. Continued

(b) $\phi = 0°$

Static pressure coefficients for x/L_n of—

Table 20. Concluded

(c) $\phi = 90°$

Static pressure coefficients for x/L_n of—

Table 21. Static Pressure Coefficients for SCF Nozzle; $L_f/d_t = 1.20; \delta_{v,y} = 10°$

(a) $\phi = -90°$

Static pressure coefficients for x/L_n of—

Table 21. Continued

(b) $\phi = 0°$

Static pressure coefficients for x/L_n of—

Table 21. Concluded

(c) $\phi = 90°$

Static pressure coefficients for x/L_n of—

Table 22. Static Pressure Coefficients for SCF Nozzle; $L_f/d_t = 1.20; \delta_{v,y} = 20°$

(a) $\phi = -90°$

Static pressure coefficients for x/L_n of—

Table 22. Continued

(b) $\phi = 0°$

Static pressure coefficients for x/L_n of—

Table 22. Concluded

(c) $\phi = 90°$

Static pressure coefficients for x/L_n of—

Table 23. Static Pressure Coefficients for SCF Nozzle; $L_f/d_t = 0.94; \delta_{v,y} = 0°$

(a) $\phi = -90°$

Static pressure coefficients for x/L_n of—

Table 23. Continued

(b) $\phi = 0°$

Static pressure coefficients for x/L_n of—

Table 23. Concluded

(c) $\phi = 90°$

Static pressure coefficients for x/L_n of—

Table 24. Static Pressure Coefficients for SCF Nozzle; $L_f/d_t = 1.46; \delta_{v,y} = 0°$

(a) $\phi = -90°$

Static pressure coefficients for x/L_n of—

Table 24. Continued

(b) $\phi = 0°$

Static pressure coefficients for x/L_n of—

Table 24. Concluded

(c) $\phi = 90°$

Static pressure coefficients for x/L_n of—

Table 1. Model Coordinates

MS, in.	r, in.
0.000	0.000
1.000	.306
2.000	.598
3.000	.876
4.000	1.140
5.000	1.390
6.000	1.627
7.000	1.850
8.000	2.060
9.000	2.257
10.000	2.440
11.000	2.611
12.000	2.768
13.000	2.919
14.000	3.045
15.000	3.164
16.000	3.271
17.000	3.364
18.000	3.446
18.500	3.481
26.000	3.514
27.000	3.570
28.000	3.614
29.000	3.645
30.000	3.664
31.000	3.670
40.890 (Metric break)	3.670
40.950	3.670
47.762 (Afterbody)	3.670
49.146	3.629
51.274	3.527
52.612	3.430
53.717	3.331
54.693	3.229
55.584	3.124
56.012 (Nozzle connect station)	3.070

Table 2. Configuration List Including Some Basic Nozzle Geometric Data

Configuration	Nozzle type	$\delta_{v,y}$	L_f/d_t
1	NVA	0°	0.94
2	NVA	0°	1.42
3	VA	0°	.94
4	VA	10°	.94
5	VA	20°	.94
6	SCF	0°	1.20
7	SCF	10°	1.20
8	SCF	20°	1.20
9	SCF	0°	.94
10	SCF	0°	1.46

Nominal nozzle data:

All nozzles:
$A_t = 6.651$ in^2
$A_e = 8.647$ in^2
$A_e/A_t = 1.30$
$(\mathrm{NPR})_{\mathrm{des}} = 4.64$

SCF nozzles:
$d_w = 3.500$ in.
$d_h = 1.900$ in.
$d_w/d_h = 1.842$

Table 3. Nozzle Coordinates

(a) NVA nozzles

$L_f/d_t = 0.94$		
MS, in.	x, in.	r, in.
56.012	0.000	3.070
56.287	.275	3.045
56.786	.774	2.930
57.281	1.269	2.790
57.795	1.783	2.620
58.331	2.319	2.433
58.906	2.894	2.250
59.533	3.521	2.035
60.229	4.217	1.810
60.622	4.610	1.670

$L_f/d_t = 1.42$		
MS, in.	x, in.	r, in.
56.012	0.000	3.070
56.412	.400	3.012
56.812	.800	2.944
57.212	1.200	2.870
57.612	1.600	2.790
58.012	2.000	2.708
58.412	2.400	2.646
58.812	2.800	2.539
59.212	3.200	2.451
59.612	3.600	2.362
60.012	4.000	2.167
60.412	4.400	2.167
60.812	4.800	2.063
61.012	5.000	2.006
61.212	5.200	1.945
61.412	5.400	1.880
61.612	5.600	1.810
61.812	5.800	1.738
61.990	5.978	1.674

Table 3. Continued

(b) VA nozzles

MS, in.	x, in.	$\delta_{v,y} = 0°$	$\delta_{v,y} = 10°$		$\delta_{v,y} = 20°$	
		r, in.	r, in.	y', in.	r, in.	y', in.
56.012	0.000	3.070	3.070	0.000	3.070	0.000
56.212	.200	3.061	3.058	.000	3.054	.000
56.412	.400	3.046	3.043	.000	3.038	.000
56.612	.600	3.026	3.027	−.001	3.022	.000
56.812	.800	3.001	3.008	−.001	3.007	−.001
57.012	1.000	2.972	2.985	.000	2.985	.000
57.212	1.200	2.940	2.956	.005	2.956	.005
57.412	1.400	2.900	2.922	.014	2.922	.015
57.612	1.600	2.847	2.885	.025	2.887	.026
57.812	1.800	2.781	2.844	.038	2.849	.040
58.012	2.000	2.710	2.795	.055	2.802	.063
58.112	2.100	2.674	2.766	.065	2.774	.079
58.212	2.200	2.635	2.735	.077	2.741	.100
58.312	2.300	2.595	2.700	.089	2.703	.126
58.412	2.400	2.555	2.664	.102	2.660	.157
58.512	2.500	2.515	2.625	.115	2.612	.192
58.612	2.600	2.475	2.585	.128	2.564	.229
58.712	2.700	2.435	2.543	.142	2.515	.266
58.812	2.800	2.395	2.499	.155	2.466	.302
58.912	3.000	2.315	2.410	.185	2.369	.376
59.212	3.200	2.235	2.317	.218	2.272	.449
59.412	3.400	2.155	2.223	.252	2.174	.522
59.612	3.600	2.075	2.128	.288	2.077	.596
59.812	3.800	1.994	2.033	.323	1.980	.669
60.012	4.000	1.914	1.938	.359	1.882	.742
60.212	4.200	1.834	1.842	.394	1.785	.816
60.412	4.400	1.754	1.747	.429	1.729	.890
60.512	4.500	1.714	1.700	.447	1.674	.927
60.612	4.600	1.674	1.674	.465		

Table 3. Concluded

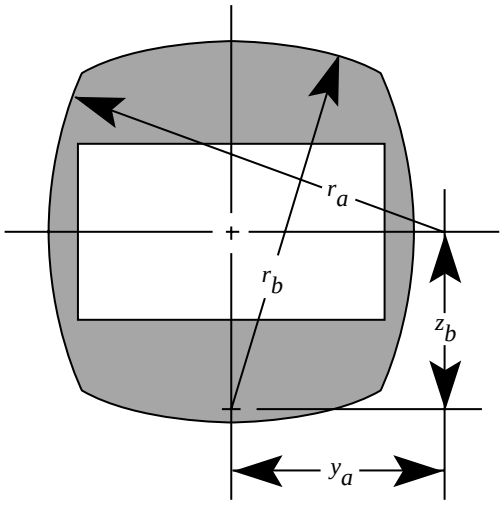

(c) SCF nozzles

L_f/d_t	MS, in.	x, in.	y_a, in.	r_a, in.	z_b, in.	r_b, in.
0.94	56.932	0.920	0.000	2.846	0.000	2.846
.94	57.612	1.600	.815	3.374	.608	3.131
.94	58.612	2.600	2.721	4.842	3.476	5.524
.94	59.612	3.600	7.701	9.383		
1.20	56.932	.920	.000	2.846	.000	2.846
1.20	57.612	1.600	.660	3.269	.513	3.081
1.20	58.612	2.600	2.403	4.287	2.296	4.455
1.20	59.612	3.600	4.663	6.544		
1.46	56.932	.920	.000	2.846	.000	2.846
1.46	57.612	1.600	.555	3.199	.444	3.046
1.46	58.612	2.600	1.641	3.973	1.738	3.981
1.46	59.612	3.600	3.391	5.413		

Table 4. Locations of External Static Pressure Orifices

$\phi = -90°$		$\phi = 0°$		$\phi = 90°$	
MS, in.	x/L_n	MS, in.	x/L_n	MS, in.	x/L_n
Configuration 1 NVA nozzle					
49.146	−1.489	49.146	−1.489	49.146	−1.489
51.274	−1.028	51.274	−1.028	51.274	−1.028
52.612	−.738	52.612	−.738	52.612	−.738
53.712	−.498	53.712	−.498	53.712	−.498
54.693	−.286	54.693	−.286	54.693	−.286
55.584	−.093	55.584	−.093	55.584	−.093
56.284	.060	56.284	.060	56.284	.060
56.787	.168	56.787	.168	56.787	.168
57.281	.275	57.281	.275	57.281	.275
57.795	.387	57.795	.387	57.795	.387
58.331	.508	58.331	.508	58.331	.508
58.906	.628	58.906	.628	58.906	.628
59.533	.764	59.533	.764	59.533	.764
60.229	.915	60.229	.915	60.229	.915
Configuration 2 NVA nozzle					
49.146	−1.148	49.146	−1.148	49.146	−1.148
51.274	−.793	51.274	−.793	51.274	−.793
52.612	−.569	52.612	−.569	52.612	−.569
53.712	−.384	53.712	−.384	53.712	−.384
54.693	−.221	54.693	−.221	54.693	−.221
55.584	−.072	55.584	−.072	55.584	−.072
56.445	.072	56.445	.072	56.445	.072
57.251	.207	57.251	.207	57.251	.207
57.995	.332	57.995	.332	57.995	.332
58.742	.457	58.742	.457	58.742	.457
59.494	.583	59.494	.583	59.494	.583
60.256	.710	60.256	.710	60.256	.710
61.984	.832	61.984	.832	61.984	.832
61.664	.945	61.664	.945	61.664	.945
Configuration 3 VA nozzle					
49.146	−1.493	49.146	−1.493	49.146	−1.493
51.274	−1.030	51.274	−1.030	51.274	−1.030
52.612	−.739	52.612	−.739	52.612	−.739
53.717	−.499	53.717	−.499	53.717	−.499
54.693	−.287	54.693	−.287	54.693	−.287
55.584	−.093	55.584	−.093	55.584	−.093
56.635	.135	56.635	.135	56.635	.135
57.523	.328	57.523	.328	57.523	.328
58.003	.433	58.003	.433	58.003	.433
58.416	.523	58.416	.523	58.416	.523
58.835	.614	58.835	.614	58.835	.614
59.286	.712	59.286	.712	59.286	.712
59.778	.819	59.778	.819	59.778	.819
60.324	.937	60.324	.937	60.324	.937

Table 4. Continued

$\phi = -90°$		$\phi = 0°$		$\phi = 90°$	
MS, in.	x/L_n	MS, in.	x/L_n	MS, in.	x/L_n
Configuration 4 VA nozzle					
49.146	−1.493	49.146	−1.493	49.146	−1.493
51.274	−1.030	51.274	−1.030	51.274	−1.030
52.612	−.739	52.612	−.739	52.612	−.739
53.717	−.499	53.717	−.499	53.717	−.499
54.693	−.287	54.693	−.287	54.693	−.287
55.584	−.093	55.584	−.093	55.584	−.093
56.687	.147	56.687	.147	56.687	.147
57.704	.368	57.704	.368	57.704	.368
58.272	.491	58.272	.491	58.272	.491
58.691	.582	58.691	.582	58.691	.582
59.076	.666	59.076	.666	59.076	.666
59.466	.751	59.466	.751	59.466	.751
59.885	.842	59.885	.842	59.885	.842
60.334	.940	60.334	.940	60.334	.940
Configuration 5 VA nozzle					
49.146	−1.493	49.146	−1.493	49.146	−1.493
51.274	−1.030	51.274	−1.030	51.274	−1.030
52.612	−.739	52.612	−.739	52.612	−.739
53.717	−.499	53.717	−.499	53.717	−.499
54.693	−.287	54.693	−.287	54.693	−.287
55.584	−.093	55.584	−.093	55.584	−.093
56.687	.147	56.687	.147	56.687	.147
57.718	.371	57.718	.371	57.718	.371
58.273	.492	58.273	.492	58.273	.492
58.642	.572	58.642	.572	58.642	.572
58.990	.647	58.990	.647	58.990	.647
59.365	.729	59.365	.729	59.365	.729
59.775	.818	59.775	.818	59.775	.818
61.461	.915	61.461	.915	61.461	.915
Configuration 6 SCF nozzle					
49.146	−1.280	49.146	−1.280	49.146	−1.280
51.274	−.884	51.274	−.884	51.274	−.884
52.612	−.634	52.612	−.634	52.612	−.634
53.717	−.428	53.717	−.428	53.717	−.428
54.693	−.246	54.693	−.246	54.693	−.246
55.584	−.080	55.584	−.080	55.584	−.080
56.181	.031	56.181	.031	56.181	.031
56.531	.097	56.531	.097	56.531	.097
56.995	.183	56.995	.183	56.995	.183
57.614	.299	57.614	.299	57.614	.299
58.157	.400	58.157	.400	58.157	.400
58.712	.504	58.712	.504	58.712	.504
59.385	.629	59.385	.629	59.385	.629
		60.027	.749		
		60.670	.869		

Table 4. Continued

$\phi = -90°$		$\phi = 0°$		$\phi = 90°$	
MS, in.	x/L_n	MS, in.	x/L_n	MS, in.	x/L_n
Configuration 7 SCF nozzle					
49.146	−1.280	49.146	−1.280	49.146	−1.280
51.274	−.884	51.274	−.884	51.274	−.884
52.612	−.634	52.612	−.634	52.612	−.634
53.717	−.428	53.717	−.428	53.717	−.428
54.693	−.246	54.693	−.246	54.693	−.246
55.584	−.080	55.584	−.080	55.584	−.080
56.181	.031	56.181	.031	56.181	.031
56.531	.097	56.531	.097	56.531	.097
56.995	.183	56.995	.183	56.995	.183
57.614	.299	57.614	.299	57.614	.299
58.157	.400	58.157	.400	58.157	.400
58.712	.504	58.712	.504	58.712	.504
		59.385	.629	59.385	.629
		60.027	.749	60.027	.749
		60.670	.869		
Configuration 8 SCF nozzle					
49.146	−1.280	49.146	−1.280	49.146	−1.280
51.274	−.884	51.274	−.884	51.274	−.884
52.612	−.634	52.612	−.634	52.612	−.634
53.717	−.428	53.717	−.428	53.717	−.428
54.693	−.246	54.693	−.246	54.693	−.246
55.584	−.080	55.584	−.080	55.584	−.080
56.181	.031	56.181	.031	56.181	.031
56.531	.097	56.531	.097	56.531	.097
56.995	.183	56.995	.183	56.995	.183
57.614	.299	57.614	.299	57.614	.299
58.157	.400	58.157	.400	58.157	.400
58.712	.504	58.712	.504	58.712	.504
		59.385	.629	59.385	.629
		60.027	.749	60.027	.749
		60.670	.869		
Configuration 9 SCF nozzle					
49.146	−1.489	49.146	−1.489	49.146	−1.489
51.274	−1.028	51.274	−1.028	51.274	−1.028
52.612	−.738	52.612	−.738	52.612	−.738
53.717	−.498	53.717	−.498	53.717	−.498
54.693	−.286	54.693	−.286	54.693	−.286
55.584	−.093	55.584	−.093	55.584	−.093
56.181	.037	56.181	.037	56.181	.037
56.531	.113	56.531	.113	56.531	.113
56.995	.213	56.995	.213	56.995	.213
57.520	.327	57.520	.327	57.520	.327
57.970	.425	57.970	.425	57.970	.425
58.431	.525	58.431	.525	58.431	.525
59.010	.650	59.010	.650	59.010	.650
		59.527	.762		
		60.045	.875		

Table 4. Concluded

$\phi = -90°$		$\phi = 0°$		$\phi = 90°$	
MS, in.	x/L_n	MS, in.	x/L_n	MS, in.	x/L_n
Configuration 10 SCF nozzle					
49.146	−1.124	49.146	−1.124	49.146	−1.124
51.274	−.776	51.274	−.776	51.274	−.776
52.612	−.556	52.612	−.556	52.612	−.556
53.717	−.376	53.717	−.376	53.717	−.376
54.693	−.216	54.693	−.216	54.693	−.216
55.584	−.070	55.584	−.070	55.584	−.070
56.181	.028	56.181	.028	56.181	.028
56.531	.085	56.531	.085	56.531	.085
56.995	.161	56.995	.161	56.995	.161
57.708	.278	57.708	.278	57.708	.278
58.345	.382	58.345	.382	58.345	.382
59.023	.493	59.023	.493	59.023	.493
59.760	.613	59.760	.613	59.760	.613
		60.527	.739		
		61.295	.865		

89-05743

L-93-08

L-93-09

L-93-10

L-93-11

L-93-12

L-93-13

L-93-14

(a) Photograph of SCF nozzle.

Figure 1. Single-engine propulsion simulation system.

(b) Sketch of simulation system. Dimensions in inches.

Figure 1. Concluded.

Figure 2. Sketches of nozzles.

Figure 3. Sketch of NVA nozzle, shown with two divergent flap lengths. Dimensions in inches.

Figure 4. Photograph of NVA nozzles.

(a) Sketch of VA nozzle, shown with two geometric yaw angles. Dimensions in inches unless otherwise noted.

(b) External contours of NVA and unvectored VA nozzles.

Figure 5. Geometry of VA nozzle.

Figure 6. Photograph of VA nozzles.

Figure 7. Sketch of SCF nozzle showing configurations with three divergent flap lengths and two geometric yaw angles. Dimensions in inches unless otherwise noted.

Figure 8. Photograph of SCF nozzles.

Figure 9. Static thrust performance of NVA, VA, and SCF nozzles. $\delta_{v,y} = 0°$.

Figure 10. Effect of divergent flap length on static thrust performance of NVA nozzle. $\delta_{v,y} = 0°$.

Figure 11. Effect of divergent flap length on static thrust performance of SCF nozzle. $\delta_{v,y} = 0°$.

(a) $M = 0.60$ to 0.95.

Figure 12. Comparison of NVA, VA, and SCF thrust-minus-nozzle-drag performance. $\delta_{v,y} = 0°$.

(a) $M = 0.60$ to 0.95.

Figure 12. Thrust-minus-nozzle-drag performance for NVA, VA, and SCF nozzles. $\delta_{v,y} = 0°$.

(b) $M = 1.20$ and 1.28.

Figure 12. Concluded.

Figure 13. Summary of thrust-minus-nozzle-drag performance for NVA, VA, and SCF nozzles. $\delta_{v,y} = 0°$.

Figure 14. Nozzle drag for NVA, VA, and SCF nozzles. $\delta_{v,y} = 0°$.

(b) $M = 0.90$.

Figure 33. Concluded.

(a) $M = 0.60$.

Figure 34. Yaw thrust-vectoring performance for VA and SCF nozzles.

(b) $M = 0.90$.

Figure 34. Concluded.

(a) Nozzle windward side.

Figure 35. Flow visualization characteristics for SCF nozzle. $\delta_{v,y} = 10°$; $M = 0.7$.

(b) Nozzle leeward side.

Figure 35. Continued.

(c) Nozzle top side.

Figure 35. Continued.

(d) Nozzle bottom side.

Figure 35. Concluded.

REPORT DOCUMENTATION PAGE

Form Approved
OMB No. 0704-0188

1. AGENCY USE ONLY *(Leave blank)*	2. REPORT DATE	3. REPORT TYPE AND DATES COVERED
	May 1993	Technical Paper

4. TITLE AND SUBTITLE
Performance Characteristics of Two Multiaxis Thrust-Vectoring Nozzles at Mach Numbers up to 1.28

5. FUNDING NUMBERS
WU 505-62-30-01

6. AUTHOR(S)
David J. Wing and Francis J. Capone

7. PERFORMING ORGANIZATION NAME(S) AND ADDRESS(ES)
NASA Langley Research Center
Hampton, VA 23681-0001

8. PERFORMING ORGANIZATION REPORT NUMBER
L-17151

9. SPONSORING/MONITORING AGENCY NAME(S) AND ADDRESS(ES)
National Aeronautics and Space Administration
Washington, DC 20546-0001

10. SPONSORING/MONITORING AGENCY REPORT NUMBER
NASA TP-3313

11. SUPPLEMENTARY NOTES

12a. DISTRIBUTION/AVAILABILITY STATEMENT
Unclassified–Unlimited

Subject Category 02

12b. DISTRIBUTION CODE

13. ABSTRACT *(Maximum 200 words)*

The thrust-vectoring axisymmetric (VA) nozzle and a spherical convergent flap (SCF) thrust-vectoring nozzle were tested along with a baseline nonvectoring axisymmetric (NVA) nozzle in the Langley 16-Foot Transonic Tunnel at Mach numbers from 0 to 1.28 and nozzle pressure ratios from 1 to 8. Test parameters included geometric yaw vector angle and unvectored divergent flap length. No pitch vectoring was studied. Nozzle drag, thrust minus drag, yaw thrust vector angle, discharge coefficient, and static thrust performance were measured and analyzed, as well as external static pressure distributions. The NVA nozzle and the VA nozzle displayed higher static thrust performance than the SCF nozzle throughout the nozzle pressure ratio (NPR) range tested. The NVA nozzle had higher overall thrust minus drag than the other nozzles throughout the NPR and Mach number ranges tested. The SCF nozzle had the lowest jet-on nozzle drag of the three nozzles throughout the test conditions. The SCF nozzle provided yaw thrust angles that were equal to the geometric angle and constant with NPR. The VA nozzle achieved yaw thrust vector angles that were significantly higher than the geometric angle but not constant with NPR. Nozzle drag generally increased with increases in thrust vectoring for all the nozzles tested.

14. SUBJECT TERMS	15. NUMBER OF PAGES
Nozzles; Nozzle drag; Thrust vectoring	109
	16. PRICE CODE: A06

17. SECURITY CLASSIFICATION OF REPORT	18. SECURITY CLASSIFICATION OF THIS PAGE	19. SECURITY CLASSIFICATION OF ABSTRACT	20. LIMITATION OF ABSTRACT
Unclassified	Unclassified		